Georgia Southern University

Digital Commons@Georgia Southern

Honors College Theses

4-23-2024

Aerodynamic Design and Analysis of a Modified 2006 Mazda Miata

William N. Recher
Georgia Southern University

Follow this and additional works at: https://digitalcommons.georgiasouthern.edu/honors-theses

 Part of the Aerodynamics and Fluid Mechanics Commons, Computer-Aided Engineering and Design Commons, and the Navigation, Guidance, Control, and Dynamics Commons

Recommended Citation

Recher, William N., "Aerodynamic Design and Analysis of a Modified 2006 Mazda Miata" (2024). *Honors College Theses*. 994.
https://digitalcommons.georgiasouthern.edu/honors-theses/994

This thesis (open access) is brought to you for free and open access by Digital Commons@Georgia Southern. It has been accepted for inclusion in Honors College Theses by an authorized administrator of Digital Commons@Georgia Southern. For more information, please contact digitalcommons@georgiasouthern.edu.

AERODYNAMIC DESIGN AND ANALYSIS OF A MODIFIED 2006 MAZDA MIATA

An Honors Thesis Submitted in Partial Fulfillment of the Requirements for Honors in the

Department of Mechanical Engineering

by

William N. Recher

Under the mentorship of *Dr. Marcel Ilie*

ABSTRACT

Aerodynamic forces developed by automobiles have destabilizing effects at high speed. These forces tend to skew toward a vehicle's rear which can present safety concerns, especially for rear-wheel-drive automobiles like the Mazda Miata. To address oversteer and high-speed instability, a vehicle's design can be tailored to bring about aerodynamic balance and improve traction. LiDAR was used to bring the physical automobile into the digital space. Then, a splitter and diffuser were added to reduce the magnitude of the destabilizing forces. Next, the size and shape of the rear-wing required to balance the vehicle was calculated using a combination of parameters from 2D and 3D analyses. Then, the rear-wing was solid modeled, and computational fluid analysis was performed on three geometry configurations. To evaluate effectiveness, the unmodified geometry was compared to the modified configuration and results were analyzed numerically. Effectiveness was recorded from the CFD model in terms of aerodynamic lift, drag, and moment. Finally, aerodynamic parameters were imported into vehicle simulation software, and performance improvements were assessed in terms of lap time reduction.

KEY TERMS: Automotive Design, Aerodynamics, Inverted Wing, Spoiler, Computational fluid dynamics, Finite element method, Finite volume method

April 2024

Georgia Southern University
Statesboro, GA

© 2024

WILLIAM N. RECHER

All Rights Reserved

ACKNOWLEDGEMENTS

I would like to thank Dr. Marcel Ilie and John Havenar for supporting this work. I would also like to thank the Department of Mechanical Engineering and the Honors College for providing students with the resources to publish research in a field of their choosing. Finally, I would like to thank my father, mother, and especially Thalia for their continued encouragement.

TABLE OF CONTENTS

ACKNOWLEDGEMENTS **vi**
TABLE OF CONTENTS **vii**

Nomenclature **viii**

1. Introduction **1**
1.1 Background **1**
1.2 Mazda Miata (MX-5) **1**
1.3 Driving Dynamics **2**
1.3.1 Lift 3
1.3.2 Moment 4
1.3.3 Drag 6

2. Methodology **7**
2.1 Overview **7**
2.2 LiDAR **8**
2.1.1 Background 8
2.1.2 Implementation 8
2.2 Computer Aided Design **10**
2.2.1 Geometry Definition 10
2.2.2 Fluid Volume 11
2.3 Computational Fluid Dynamics **12**
2.3.1 Theory 12
2.3.2 Model 13
2.3.3 Boundary Conditions 14
2.3.4 Spatial Discretization 15

3. Results **18**
3.1 Preliminary Analysis **18**
3.2 Aerodynamic Balancing **20**
3.2.1 Approach 20
3.2.2 2D Analysis 21
3.2.3 Balancing Script Outputs 22
3.2.4 CFD Tabular Results 23
3.2.5 CFD Trends and Velocity Visualization 24
3.2.6 CFD Trends and Pressure Visualization 28

4 Conclusion **31**
4.1 Contextualizing Results **31**
4.2 Closing Remarks **33**

REFERENCES **34**

NOMENCLATURE

α	Angle of attack
ρ	Density
a	Speed of sound
b	Semi-span
c	Chord length
g	Gravitational acceleration
t	Time
v	Velocity
τ	Stress tensor
F	Body forces
L	Lift
D	Drag
M	Moment
C_L	Lift coefficient
C_D	Drag coefficient
C_M	Moment coefficient
C_p	Pressure coefficient
l_{ref}	Reference length
A_{ref}	Reference area
BHP_D	Brake horsepower consumed by drag
Ma_∞	Freestream Mach number
V_∞	Freestream Velocity

1. INTRODUCTION

1.1 Background

Automobiles tend to produce aerodynamic lift at high speed and this force can upset driving dynamics when they matter most. Safety concerns arise when aerodynamic effects reduce the traction available, increasing the likelihood of an uncontrolled slide. This places the driver and passengers at risk of encountering a high-speed collision.

For the purposes of this thesis, vehicle performance will be defined in terms of cornering acceleration, stopping acceleration, and top speed. In the work that follows, the author seeks to apply motorsport design principles to a passenger automobile with the expectation of achieving safety and performance improvements.

1.2 Mazda Miata (MX-5)

The Mazda Miata is a rear wheel drive two-door convertible which made its debut in 1989. In the thirty-five years since, four generations (NA, NB, NC, and ND) have been offered for sale. The subject of this analysis falls into the third (NC1) generation and can be seen in Figure 1. This vehicle is equipped with a 2.0 Liter inline four-cylinder engine, a six-speed manual transmission, a limited slip differential, and a fabric convertible roof. The original 17” x 7” alloy wheels have been replaced with 17” x 9” wheels which are configured with -2.5° of camber. Also, the vehicle’s original struts and springs have been replaced with ride-height adjustable suspension.

In the analysis which follows, the 17” x 9” wheels and tires have been incorporated into all configurations. Also, ground clearance was measured at the pinch welds, and was modelled at 4.00 inches front and 4.25 inches rear for all configurations.

Figure 1. 2006 Mazda Miata (NC1)

1.3 Driving Dynamics

Automobile maneuvers can be broken down into straight-line, braking, and cornering components, and in each of these cases an acceleration limit exists. If this limit is exceeded, then no matter how much input is commanded from the driver, the vehicle will fail to respond. This behaviour can be explained by introducing the concept of a limit of static friction.

Under normal operating conditions, automobile tires roll across a ground surface. However, if the driver performs an emergency stop then it is possible to interrupt tire rotation, or “lock up” the tires, while the vehicle is still in motion. In this example the limit of static friction has been exceeded and the tires slide across the ground plane. The limit of static friction can be plotted using a traction circle as shown in Figure 2.

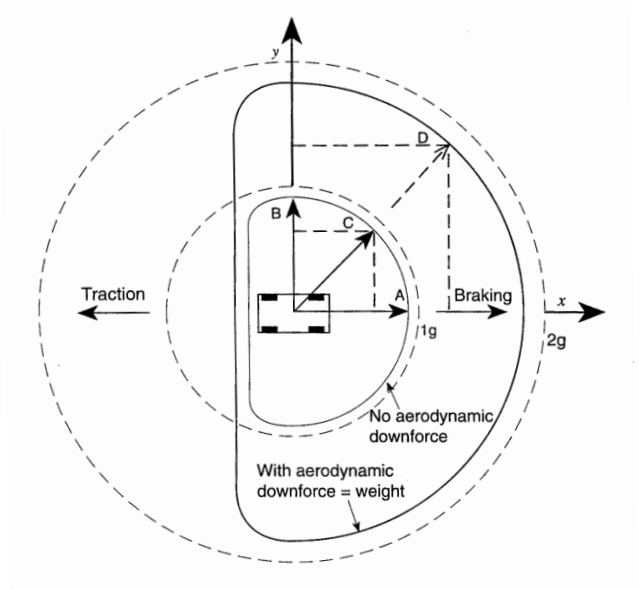

Figure 2. Traction Circle [1]

This limit of static friction depends on a variety of factors including tire chemistry, moisture, temperature, road roughness, and tire load. In Figure 2, the vehicle is travelling in the -x direction, and the emergency braking example would occur along vector A.

1.3.1 Lift

Aerodynamic forces generate a lifting effect on passenger vehicles at speed. Aerodynamic lift reduces the reaction force between the tire and the road. This reduces tire deformation, causing less keying to occur between the compliant rubber and the ridges and valleys of the road's surface. Drivers experience this phenomenon as a loss of traction. Lift can be described in terms of dynamic pressure, reference area, and lift coefficient as shown in Eq. (1). Lift coefficient can be determined experimentally, or numerically.

$$L = C_L A_{ref} \frac{1}{2} \rho {v_\infty}^2 \tag{1}$$

1.3.2 Moment

The Miata was designed with 50% front 50% rear static weight distribution to achieve desirable handling characteristics. Unfortunately, as with most vehicles, the Miata does not produce a balanced lift distribution. Instead, aerodynamic lift is concentrated at the rear, resulting in uneven tire loads. The Miata is rear-wheel-drive and in this case the most pronounced lifting effect occurs at the driven wheels. If left unchecked this may induce high speed oversteer, a behaviour widely considered to be dangerous and unpredictable. The unbalanced "stock" vehicle can be seen in Figure 3.

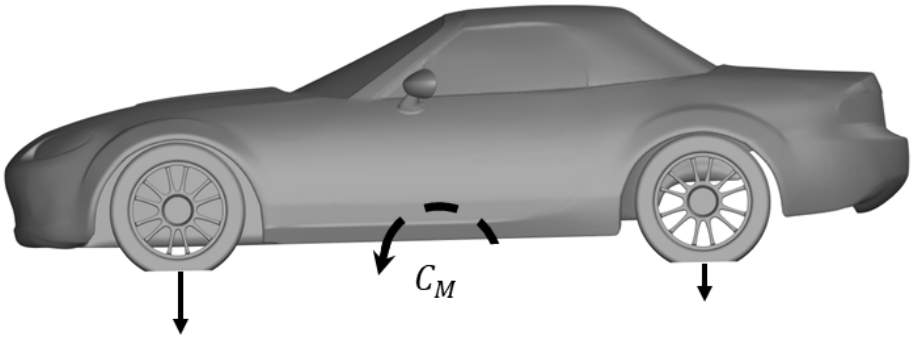

Figure 3. Unbalanced configuration (*Case I*)

However, modifications can be designed to balance the vehicle as shown in Figure 4. First, balance can be assessed by calculating rotational moment about the midpoint between the front and rear tires. Because the Miata possesses a 50/50 static weight distribution, the sum of moments about the midpoint must be equal to zero.

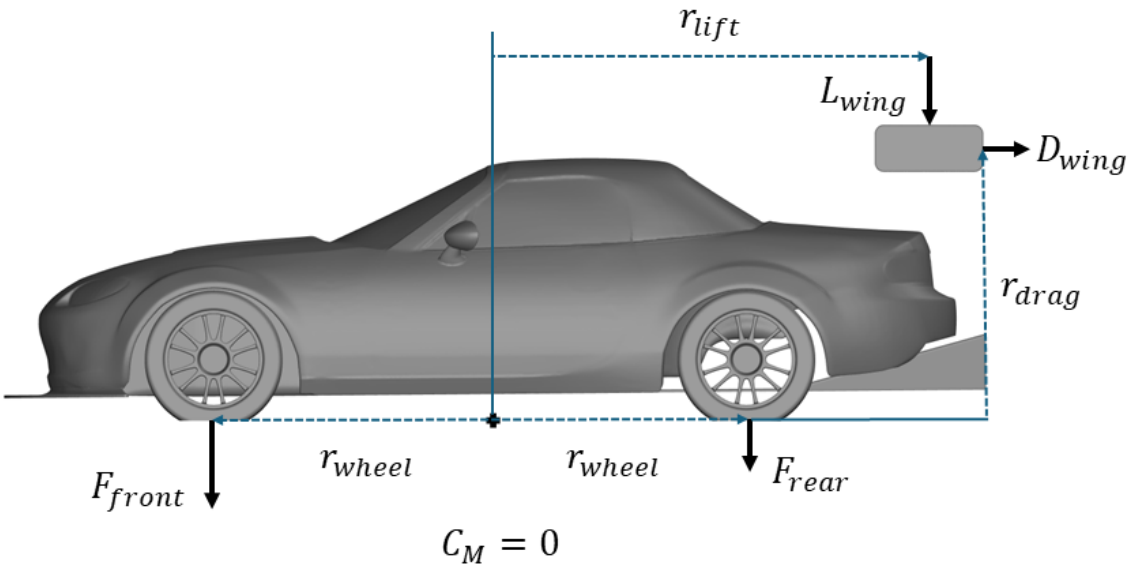

Figure 4. Balanced configuration (*Case III*)

Aerodynamic moment is described using a moment coefficient, reference area, reference length, and dynamic pressure as shown in Eq. (2). Similar to the force coefficients, the moment coefficient is typically derived through wind-tunnel experimentation, or through numerical analysis. Moment about a balanced vehicle center is shown in Eq. (3).

$$M = C_M A_{ref} l_{ref} \frac{1}{2} \rho {v_\infty}^2 \tag{2}$$

$$\sum M_j = 0 \tag{3}$$

1.3.3 Drag

Aerodynamic drag is another consideration for automotive design. The Miata's limited brake horsepower (P = 170 bhp) [2], and a large drag coefficient (C_D = 0.390) [3] limit acceleration at high speed. Aerodynamic drag also contributes to fuel-economy losses, affecting casual drivers and endurance racers alike. Remaining drag-conscious is popular in high-speed motorsports because drag limits acceleration on straight sections of track where overtakes are most likely to occur among amateur drivers. In this analysis, modifications will be explored which reduce lift and moment while limiting an associated drag penalty. The equation for aerodynamic drag is shown in Eq. (4). A dimensional equation for horsepower lost to aerodynamic drag is shown in Eq. (5) [1]. Velocity (v_∞) is in terms of [m/s] and horsepower consumed by drag (BHP_D) is in terms of imperial horsepower [hp].

$$D = C_D A_{ref} \frac{1}{2} \rho {v_\infty}^2 \tag{4}$$

$$BHP_D = \frac{C_D A_{ref} {v_\infty}^3}{1{,}225} \tag{5}$$

In low-speed motorsport events like autocross, it is common to neglect drag in its entirety. In these settings, vehicles are traction-limited for the duration of the event, so lift reduction becomes the primary concern. Because the subject vehicle is intended for high-speed tracks and occasional highway use, drag is being considered in this analysis.

2. METHODOLOGY

2.1 Overview

The design and analysis process has been described using a methodological flow chart shown in Figure 5. The details for each step have been described in the following sections.

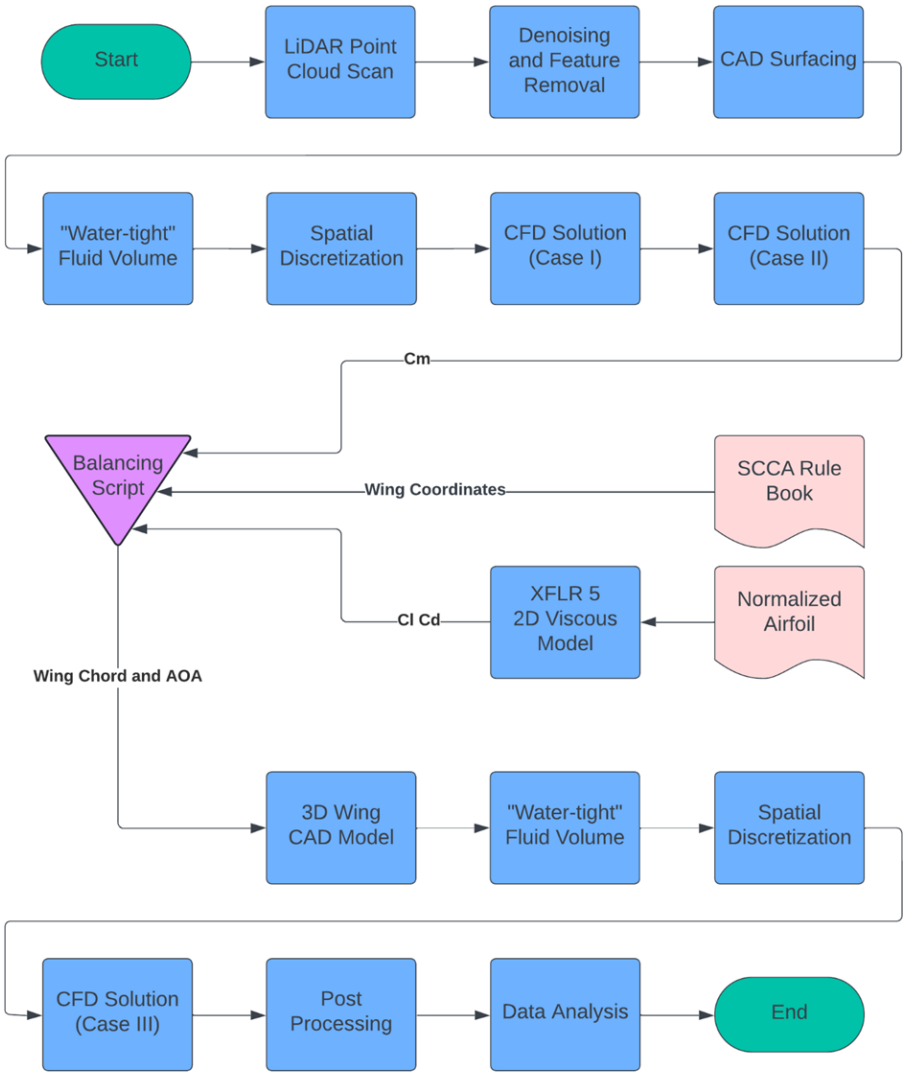

Figure 5. Methodology flow chart

2.2 LiDAR

2.1.1 Background

Light Detection and Ranging (LiDAR) technology has rapidly matured as hardware becomes higher quality less expensive. Applications range from facial recognition to aerial terrain mapping and even self-driving cars.

LiDAR technology makes use of the same fundamental principle as Radio Detection and Ranging (RaDAR) and Sound Navigation and Ranging (SoNAR). A signal wave is generated and emitted, then the wave reflected off the environment before being measured by a sensor in a known position. The vector and time delay associated with the reflected wave are post-processed to determine the position of the reflecting object. Modern LiDAR technology allows users to collect three-dimensional point-cloud data. This information can be post-processed using mesh editing software to join scan files and discard extraneous data points. Then a contiguous surface can be fitted to the point cloud data set and smoothed according to the user's preferences.

2.1.2 Implementation

The vehicle was lifted onto jack stands and LiDAR scanned in quadrants, first from above, and then from below. Scanning large objects, especially vehicles, in multiple steps reduces the likelihood of tracking errors which force the operator to restart the scanning procedure. It should also be noted that LiDAR technology has the tendency to collect low-quality data when scanning reflective surfaces like high-gloss paint. Some have distributed talcum "baby" powder and tracking targets over reflective surfaces to mitigate these issues.

In this case, small amounts of dust from typical use made object scanning reasonably efficient.

Commercial LiDAR scanners designed for automotive use are available, but an iPhone 13 Pro was used in this case due to financial considerations. Point cloud data was collected using the finest detail setting available in a free-to-use application, and a rolling dolly (mechanic's creeper) was used while underneath the vehicle to keep the operator's hands free to use the scanner. Once the scanning process was complete, point cloud data was transferred to a personal computer for post-processing.

Scan files were "stitched" together using an open-source mesh editing software named MeshLab. Erroneous data points were discarded, a tessellated surface was generated, and the surface was smoothed to reduce unnecessary faceting. Then, the surface was exported as a stereolithography file and imported into computer aided design software. The smoothed surface of the undercarriage is shown in olive-green in Figure 6.

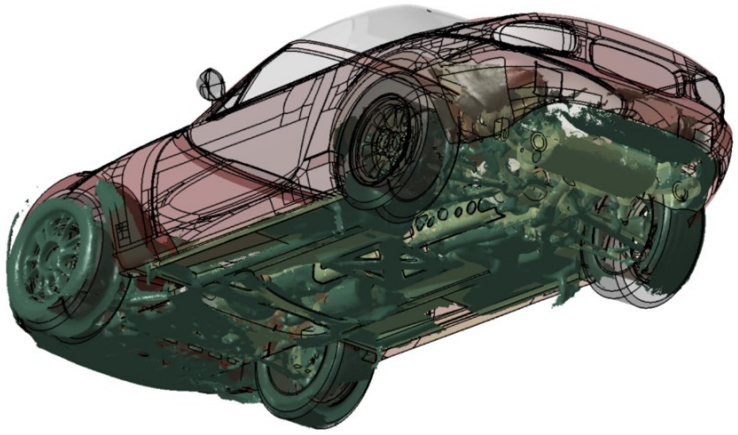

Figure 6. Undercarriage scan, three-quarter view

2.2 Computer Aided Design

2.2.1 Geometry Definition

Reference surfaces for a 2006 Mazda Miata were located using the OnShape user library and imported into the CAD model [4]. These surfaces were likely generated using graphic design software (Blender or equivalent) for racing simulator video games. These surfaces describe the form of the vehicle, but fail to resolve intersections and panel gaps which make the geometry unusable for numerical analysis. The reference surfaces also fail to describe the vehicle's undercarriage.

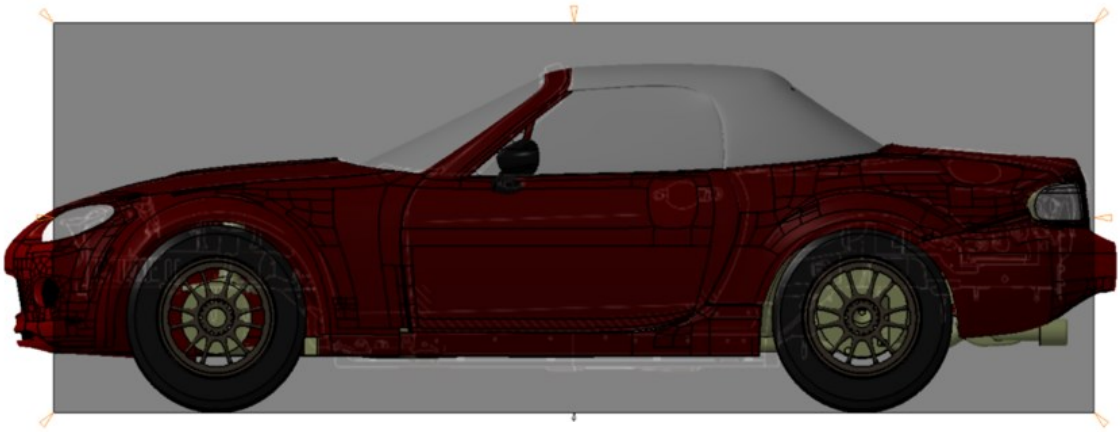

Figure 7. Geometry validation

Before proceeding, reference surfaces, scan data, and Mazda's orthographic projections were overlaid and checked for agreement. All three data sources agreed within reasonable limits as shown in Figure 7. From this point, CAD software was used to surface model the vehicle's undercarriage using the LiDAR scan surface as a reference. Then, details like door handles and the center high mounted stop light were discarded. Recesses in the front bumper for the grille and fog lights were smoothed over. Finally, surfaces were extended to reduce panel gaps to 0.100" or less. Then, an inside face was modelled for thin

components like the rear bumper and the front/rear fenders. These components were converted into solid models and their sharp edges were rounded. These steps simplified the geometry discretization process in the work that follows. Results from the geometry simplification are shown in Figure 8.

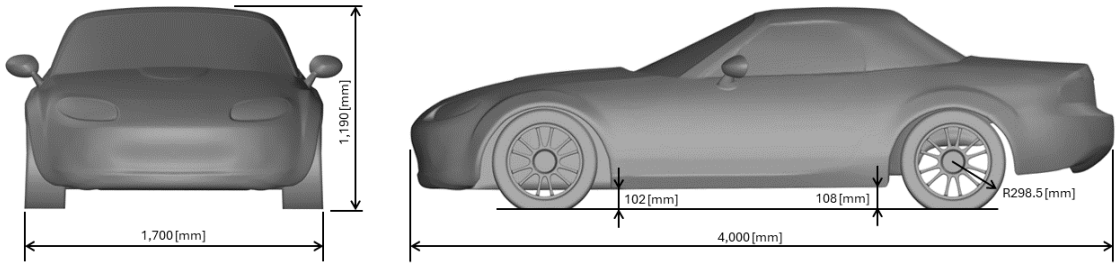

Figure 8. Vehicle dimensions

The vehicle's original suspension has been replaced and the ride height reduced. Technical publications from Mazda list minimum ground clearance as 4.75 inches or 117 millimeters [2] while minimum ground clearance for this analysis was 102 millimeters. Research literature has established a negative correlation between ground clearance and downforce [5], i.e. as ground clearance is reduced downforce increases. For this analysis, the effects of varying ride height were not studied, and all geometry configurations share common ground clearances.

2.2.2 Fluid Volume

CAD surfaces were then imported into ANSYS SpaceClaim and an enclosure was modelled as shown in Figure 9. Offsets from the vehicle to the boundaries of the enclosure were based on the published literature [6] [7]. A solid model of the car was developed using a surface wrapping feature [8]. This "shrink-wrap" tool allows users to generate a solid body from a set of discontinuous surfaces, enabling users to generate usable CFD geometry

from “messy” CAD data. The user is prompted to input a gap size and feature angle to control geometry refinement [8]. In this case, a 3 [mm] gap was implemented, and the angle threshold was left unselected. The shrink-wrap tool was executed, and the output body was inspected for irregularities. Finally, adjacent tessellations were merged to reduce geometric complexity.

Now that a “watertight” vehicle domain had been generated, a Boolean operation was used to subtract the vehicle from the enclosure. The remaining solid represents the fluid volume of air within the virtual wind tunnel. Finally, surfaces were group-selected and labelled in the feature tree for use while setting up the CFD model.

2.3 Computational Fluid Dynamics

2.3.1 Theory

Computational Fluid Dynamics (CFD) is a field of study which seeks to explain flow patterns by implementing the governing laws of fluid motion. In their present form, the governing equations are defined by Navier and Stokes, and these equations describe conservation of mass, momentum, and energy through a fluid continuum with compressible and viscous effects.

The Navier-Stokes equations are partial differential equations with no proven closed-form solution. Instead, this equation set is most often solved using numerical iteration and a process termed Reynolds averaging. Here, flow patterns are decomposed into averaged and fluctuating components where the averaged components are solved directly by the solution algorithm, and fluctuating (viscous) components are approximated

using a turbulence model. This closes the system of equations and allows the solver to compute fundamental flow variables including pressure and velocity. From here, complex field variables including vorticity (a measure of a flow's rotation) can be derived. For the purposes of this analysis, the finite volume method was used to apply Reynolds averaging to the fluid domain.

To simplify the mathematical model, freestream Mach number can be calculated using Eq. (6). Because Mach number is less than 0.3 ($Ma_\infty < 0.3$), the flow can be considered incompressible, and the energy equation can be omitted. The Navier Stokes equations for mass and momentum remain and are listed in Eq. (7) and Eq. (8) respectively [9].

$$Ma_\infty = \frac{V_\infty}{a} \tag{6}$$

$$\frac{\partial \rho}{\partial t} + \nabla \cdot (\rho \vec{v}) = 0 \tag{7}$$

$$\frac{\partial}{\partial t}(\rho \vec{v}) + \nabla \cdot (\rho \vec{v} \vec{v}) = -\nabla p + \nabla \cdot (\bar{\bar{\tau}}) + \rho \vec{g} + \vec{F} \tag{8}$$

2.3.2 Model

The Ansys Fluent 2022 R2 pressure-based solver was used in conjunction with an unsteady Reynolds Averaged Navier-Stokes (uRANS) formulation to simulate the flow field around a half-model. The SST $k - \omega$ eddy viscosity model was selected for this study because it has been proven to accurately predict flow separation under adverse pressure gradients [10], and it is cited in the literature for automotive fluid analysis [6]. The closure

constants used were: $\alpha_\infty{}^* = 1,\ \alpha_\infty = 0.52,\ \beta_\infty{}^* = 0.09, \alpha_1 = 0.31,\ \beta_1 = 0.075, \beta_2 = 0.0828, \sigma_{k1} = 1.176, \sigma_{k2} = 1.0, \sigma_{\omega 1} = 2.0, \sigma_{\omega 2} = 1.168.$

All simulations were initialized by applying the free-stream velocity to the entire fluid volume. Then a steady state RANS simulation was run for 1,000 iterations. Finally, unsteady RANS was run for 500 time-steps, totalling 1 second of flowtime. Force coefficients were assessed using the projected frontal area of the half-model $A_{ref} = 0.81$ [m^2] and the overall length of the vehicle $l_{ref} = 4.0$ [m].

2.3.3 Boundary Conditions

A velocity inlet was applied with varying magnitude v_∞ = [26.82, 44.70, 62.59] [m/s] which corresponds with 60, 100, and 140 miles per hour respectively. Then, a pressure outlet was applied to the outflow surface. Symmetry boundary conditions were applied to the vehicle symmetry plane, and to the flow field's limits as shown in Figure 9.

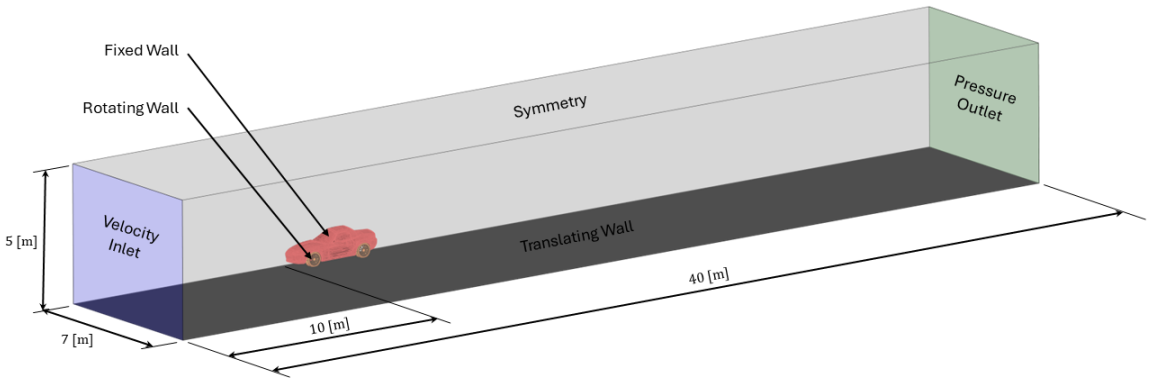

Figure 9. General boundary conditions

Wall boundary conditions were used to define the vehicle's bodywork, wheels, tires, and the ground plane, all of which were applied with a no-slip condition. The ground

plane was assigned translational motion equivalent with the free stream velocity (v_∞). Wheels and tires were assigned rotational motion with angular speed calculated using the free stream velocity and tire radius shown in Eq. (9). Tire radius $r = 0.298$ [m] was used to calculate the rotational speed $\omega =$ [89.87, 149.79, 209.70] [rad/s]. Boundary motion has been illustrated in Figure 10. Results were generated using a moment convention defined by the right-hand rule into the page which is also shown in Figure 10.

$$\omega = \frac{v_\infty}{r} \tag{9}$$

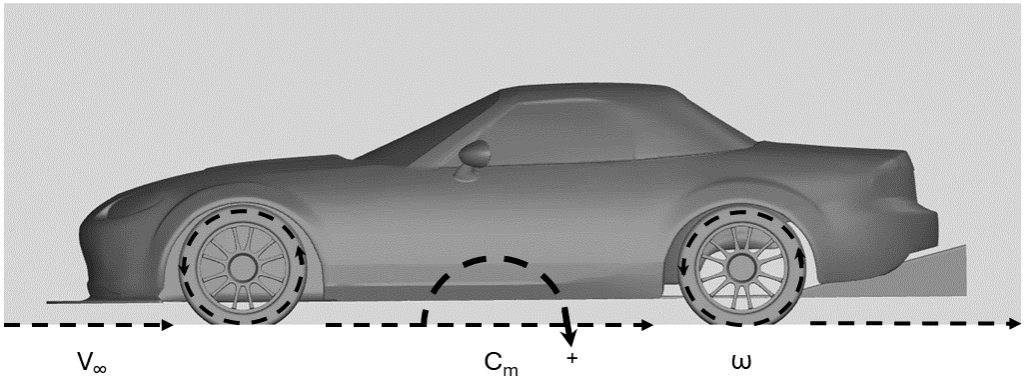

Figure 10. Moving boundary conditions

2.3.4 Spatial Discretization

A volume mesh was generated to break the fluid volume into finite volume cells. This process is termed spatial discretization, which is a critical step for generating accurate results. Ansys Fluent Meshing 2022 R2 was used for all three cases.

Refinement settings were applied with some deviation in the minimum surface size and intermediate field size. Cell count remained less than 15 million for each case due to a hardware limit of 64 GB of DRAM. Future work can be done to eliminate cusps in the

geometry near the splitter/front bumper intersection which would allow the minimum cell size to increase, and refinement to be reintroduced to the intermediate refinement region.

A ploy-hex core meshing algorithm was used in conjunction with prismatic inflation layers to generate the finite volume mesh. Twelve inflation layers were used to refine the viscous sublayer, and first layer height was configured for use with a wall-function. First layer height was calculated for a target y-plus equal to forty ($y^+ = 40$), a free-stream velocity of sixty miles per hour ($v_\infty = 26.82$ [m/s]), and the vehicle's overall length of four meters ($l_{ref} = 4.0$ [m]). Mesh sizes for the stock (*Case I*) configuration are listed in Table 1 and plotted in Figure 11.

Table 1. Mesh settings

Region	Size [mm]
Surface mesh	10
First layer height	1.2
Near field	25
Intermediate	50
Far field	250

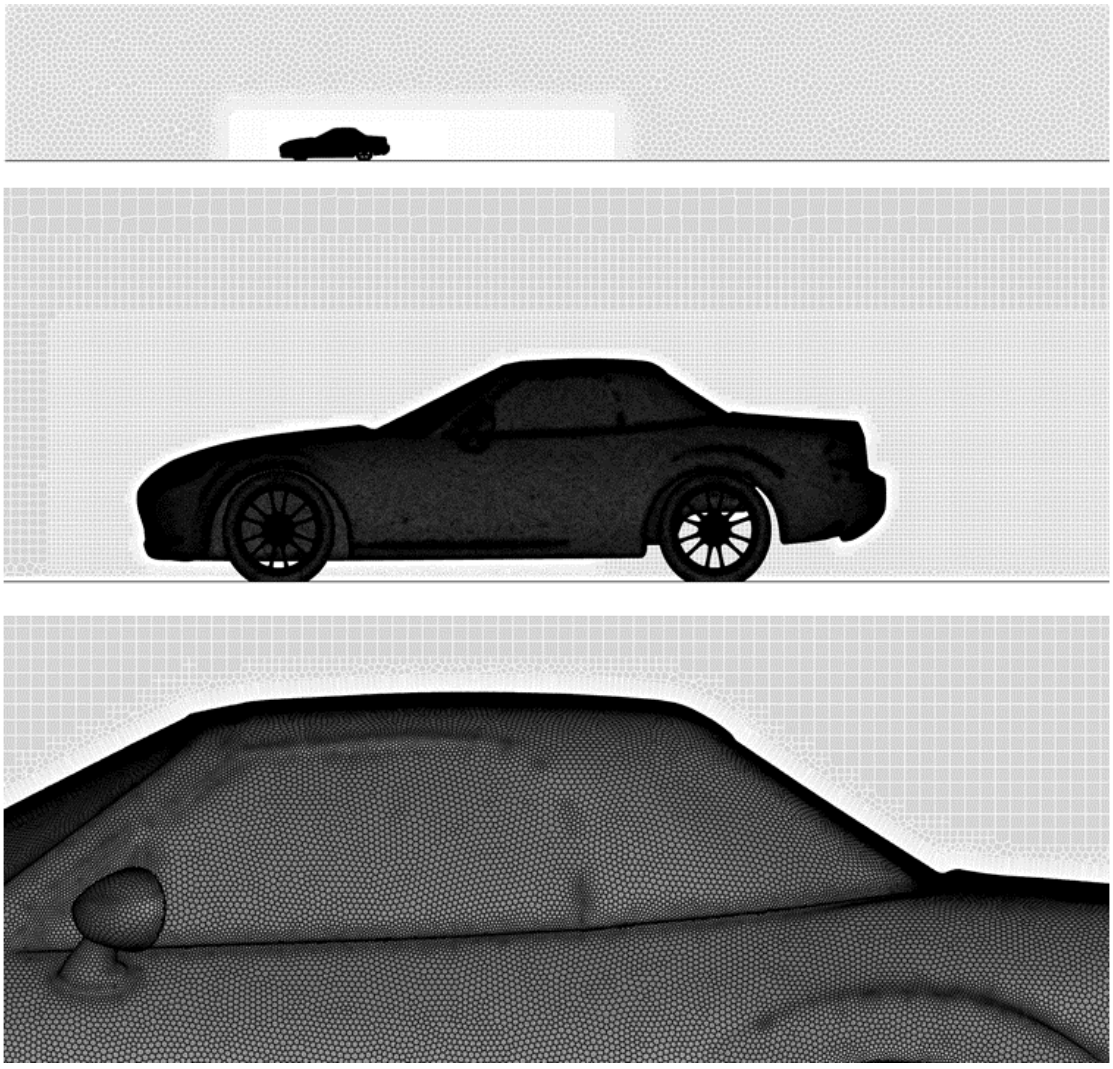

Figure 11. Spatial discretization

3. RESULTS

3.1 Preliminary Analysis

To begin, case files were generated for the stock (*Case I*), and partially modified (*Case II*) configurations. *Case I* and *Case II* were analysed using a free-stream velocity of sixty miles per hour ($v_\infty = 26.82$ [m/s]) and an unsteady RANS formulation. *Case I* was expected to match experimental drag data [3], and *Case II* was expected to reduced lift, drag, and moment coefficients from the stock configuration.

Force coefficients were time-averaged across one second of flow time and recorded in Table 2. Drag coefficient from the stock (*Case I*) configuration was compared against full-scale wind tunnel results [3], and percent error was calculated to be less than 1%.

Table 2. Preliminary results

Case	**Configuration**	**Cell Count**	C_L	C_D	C_M
I	Stock	5.6 million	0.084	**0.393**	-0.046
II	Stock + Splitter + Diffuser	12.5 million	-0.162	0.360	-0.171

Results from the partially modified (*Case II*) configuration showed reduced lift and drag coefficients as expected. A reduction of the moment coefficient is also expected because the front splitter combined with the uneven lift distribution, which resulted in a greater diving moment overall. To balance the vehicle, the magnitude of the moment coefficient must be reduced, and this has been accomplished by incorporating a rear wing.

To design an effective wing, the velocity field was sampled at the intended location. Velocity vectors were plotted at five locations across the span and are shown in Figure 12. Because the vectors are well-aligned, it was decided that wing-twist was not necessary. However, if the wing were positioned closer to the ground plane, then a spanwise velocity differential would be expected due to the three-dimensional effects of the cabin's wake. In this hypothetical, the wing could be twisted to maintain a constant angle of attack across the span.

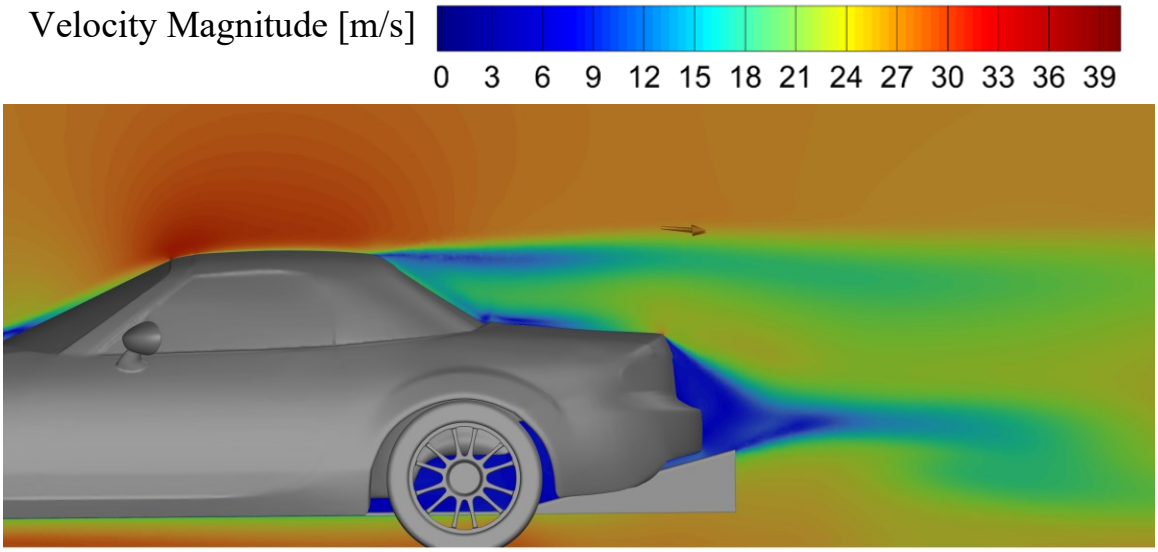

Figure 12. Velocity contours with spanwise vectors (Case II)

3.2 Aerodynamic Balancing

3.2.1 Approach

To balance the vehicle, a rear-wing was to be added to minimize the magnitude of the moment coefficient. To size the wing appropriately, a script was written to find the most-efficient angle of attack and required chord length for a given airfoil. Script input parameters are shown in Figure 13. The Sports Car Club of America (SCCA) rulebook was referenced when sizing and positioning aerodynamic features. The semi-span of the wing was set equal to the vehicle width excluding side mirrors ($b = 850[mm]$), and wing position was established so the top of the wing assembly was no more than 6 inches (152 [mm]) above the roofline.

```
vInf    =  60          ; % [mph] speed
alpha   =   3          ; % [degrees] angle of attack
rho     = 1.225;         % [kg*m^-3] density
b       = 0.85;          % [m] semi-span
wngPos  = [3.84 0 1.225]; % [m] wing position in global coordinates
cm      = -0.17;         % moment coefficient of the car
Lref    = 4;             % [m] car refrence length
Aref    = 0.8126937;     % [m^2] half-car refrence area
```

Figure 13. Balancing script inputs

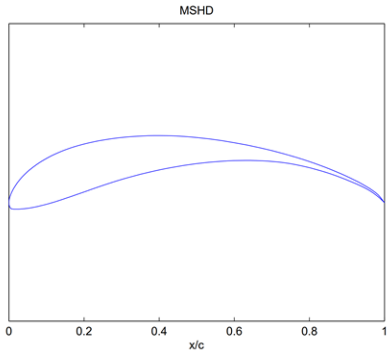

Figure 14. Motor Sports High Downforce airfoil [11]

A list of high-performance airfoils ($\max(C_l) > 2.0$) were evaluated for maximum lift coefficient, maximum lift to drag ratio, and stall characteristics. The Motor Sports High Downforce (MSHD) airfoil [11] was selected based on these considerations and is shown in Figure 14. This airfoil is highly cambered with a thin trailing edge which can pose manufacturability concerns. These concerns were excluded from this analysis.

3.2.2 2D Analysis

A 2D viscous analysis was done using an open source CFD software program named XFLR5. The optimization function of XFLR5 was used to check for improvements, but the optimization function only returned results within 5% of the original geometry. Because the MSHD profile has been extensively modeled and empirically tested, the unmodified MSHD profile was chosen for this design. XFLR5 was utilized to generate force coefficient data which is plotted in Figure 15. Wing efficiency was calculated by dividing the lift coefficient by the drag coefficient for each angle of attack, and this data can be seen in Figure 16.

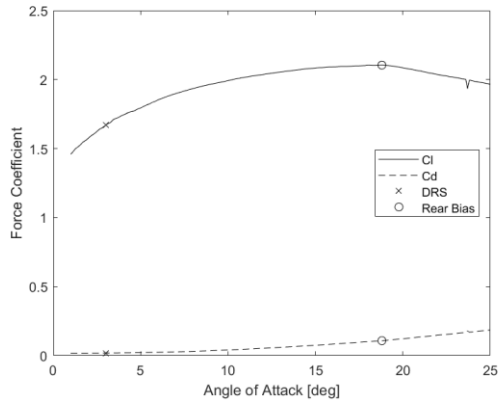

Figure 15. Force coefficients

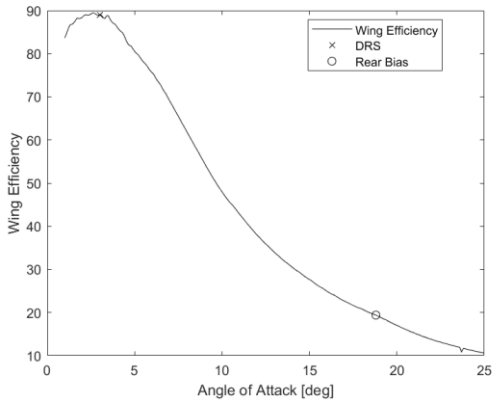

Figure 16. Wing Efficiency

Two points of interest have been chosen from the 2D analysis labelled “DRS” and “Rear Bias”. DRS points represent a reduced-drag high-efficiency wing configuration inspired by Formula One. In motorsport DRS, or drag reduction systems, are intended only to be operated in straight, high-speed, sections of track. This system is designed to give drivers a slight advantage to perform an overtake before the next corner. In this analysis, a aerodynamically balanced vehicle configuration has been chosen as the standard operating

configuration and labelled DRS. The corresponding angle of attack for this configuration ($\alpha = 3°$) was used for the remainder of this analysis.

Points labelled "Rear Bias" represent a high angle of attack, maximum-downforce configuration ($\alpha = 18.8°$) intended to increase rear tire loads and reduce the likelihood of oversteer. This configuration could be useful to a novice driver with limited training on oversteer recovery. The rear bias configuration is also a convenient reference position when tuning aerodynamic balance in situ.

3.2.3 Balancing Script Outputs

A balancing script was written to combine set values of wing position, angle of attack, and velocity, with *Case II* moment coefficient, and 2D airfoil lift and drag data. *Case II* aerodynamic moment was summed with the moments produced by wing lift and drag about the wheelbase center as shown in Figure 4 [12]. Then, this sum of moments was set equal to zero and the wing chord was solved as the output parameter. Finally, lift and drag forces were calculated and displayed to the user.

Using the DRS configuration ($\alpha = 3°$), required chord length was calculated to be 8.272 inches ($c = 210\ [mm]$). At 60 miles per hour or 26.8 [m/s], the wing was estimated to produce 59 pounds-force of downforce, and less than 1 pound-force of drag for a wing efficiency of 89. Subjecting this same chord length to the rear bias configuration ($\alpha = 18.8°$) predicted 79 pounds-force of downforce, and 4 pounds-force of drag for a wing efficiency of 19.

To account for inefficiencies neglected from the 2D analysis, like lift-induced drag and the wake of the passenger compartment, the chord length was increased (or oversized) to 9 inches ($c = 229\ [mm]$), an increase of 8.8%. The 9-inch airfoil was modelled in 3D using CAD software and is shown in Figure 17. As previously mentioned, velocity vectors were potted for *Case II* at the intended wing location. These vectors showed no change of angle of attack with respect to spanwise position, so wing twist was not incorporated into the wing design. End plates were also added to the wing assembly to limit wingtip vortices and improve wing effectiveness.

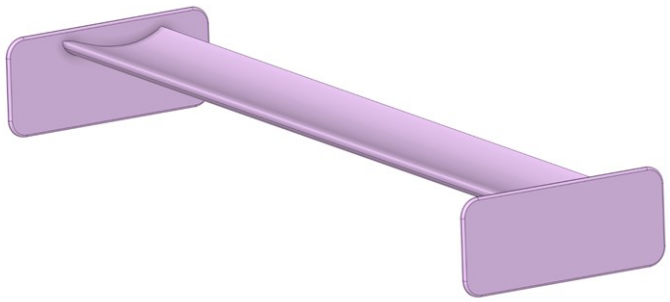

Figure 17. Wing assembly

The wing assembly from Figure 17 was added to the Case II geometry configuration and labeled "*Case III*". *Case III* included the vehicle's original bodywork with the addition of a 6-inch splitter, 12° diffuser, and balancing wing assembly. All three geometry configurations, *Case I*, *Case II*, and *Case III* were analyzed in 3D using Ansys Fluent 2022 R2. Results from this analysis are detailed in the following subsection.

3.2.4 CFD Tabular Results

Case I, *Case II*, and *Case III* geometries were meshed as discussed in the Methodology section, and each configuration was analysed at three free-stream velocities.

Just as shown in Table 2, all results for Table 3 were calculated using an unsteady RANS formulation and time averaged over one second of flowtime. It should be noted that the increase in cell count from case to case was largely due surface abnormalities introduced by the added geometry, especially near the front splitter/bumper intersection. Future work can be done to smooth this transition to increase minimum cell size, and reduce computational cost.

Table 3. Final case matrix

Case	**Configuration**	**Cell Count**	**60 [mph]**			**100 [mph]**			**140 [mph]**		
			C_L	C_D	C_M	C_L	C_D	C_M	C_L	C_D	C_M
I	Stock	5.6 M	0.084	0.393	-0.046	0.129	0.407	-0.061	0.158	0.420	-0.060
II	Stock +Splitter +Diffuser	12.5M	-0.162	0.360	-0.171	-0.162	0.353	-0.161	-0.154	0.352	-0.160
III	Stock +Splitter +Diffuser +Wing	13.7M	-0.519	0.382	-0.031	-0.525	0.373	-0.023	-0.530	0.369	-0.019

3.2.5 CFD Trends and Velocity Visualization

A few patterns can be noticed in the data from Table 3. First, force and moment coefficients vary with speed, especially for the stock (*Case I*) configuration. This phenomenon has been labelled "Reynolds dependency" in the literature [6] and seems to be common automotive analysis. *Case I* differs from *Case II* and *Case III* in that the drag coefficient increases with speed for *Case I*, while drag coefficient decreases with speed for

Case II and *Case III*. The modified *Case II* and *Case III* configurations agree with the trend of decreasing drag coefficient with respect to speed established in the literature [6].

Second, lift and moment coefficients increase in magnitude with respect to speed for *Case I*. This indicates the destabilizing forces *increase* at a rate greater than velocity squared ($v_\infty{}^2$) for the unmodified vehicle. However, for the modified *Case III* geometry, lift, drag, and moment coefficients *decrease* with respect to speed. This pattern indicates the modified vehicle trends toward stability at high-speed.

Third, at each speed, there is a reduction in the lift coefficient, a trend toward zero for the moment coefficient, and a small reduction in the drag coefficient from the unmodified (*Case I*) to the modified (*Case III*) configuration. Reductions in lift and moment coefficients indicate performance improvements by increasing the limit of static friction and reducing the likelihood of oversteer respectively. Also, a small reduction in drag coefficient makes the vehicle slightly faster on straight sections of track while improving fuel efficiency.

Velocity contours at 60 miles per hour are shown in Figure 18 - Figure 20 and conclusions have been drawn from these results. First, it can be noticed that the wake beneath the rear bumper has been nearly eliminated from *Case I* to *Case II*. This effect was generated by the rear diffuser and is accompanied by an appreciable reduction of the drag coefficient. It should be noted that a flat floor was implemented to span the gap between the passenger floorboards and the diffuser entrance, which was done to feed the diffuser clean air. While care was taken to avoid powertrain and suspension components, it should

be noted that this geometry represents a best-case scenario because diffuser effectiveness greatly depends on the flow regime of the incoming air.

Second, the wake, or the volume of disturbed air, occupies more vertical space in *Case III* than *Case I* which can be visualized using the scale positioned downstream of the vehicle in Figure 18 - Figure 20. The increase in wake height coincides with a reduction in the lift coefficient from *Case I* to *Case III* as one would expect. Because more air is directed upwards, conservation of momentum would dictate a reduction in the lift coefficient. This observation agrees with the data from Table 3.

Third, air separates from the front splitter immediately following the leading edge. This can be seen in the comparison between the modified (*Case III*) configuration, and the stock front bumper from *Case I*. It seems the region between the splitter and the ground plane is largely supplied by the high-pressure stagnation region from above. As air makes its way around the sharp leading edge, the boundary layer is tripped, and the flow detaches almost immediately. This detached, turbulent flow is most-likely responsible for the reduction of air velocity beneath the vehicle across these two cases. By applying Bernoulli's principle, a reduction of air velocity would predict an increase in static pressure. Tying this all together, the sharp leading edge of the splitter likely causes a downforce inefficiency due to reduced air velocity beneath the vehicle. If the splitter's leading edge were rounded, then perhaps this inefficiency could be reduced, and more downforce could be generated.

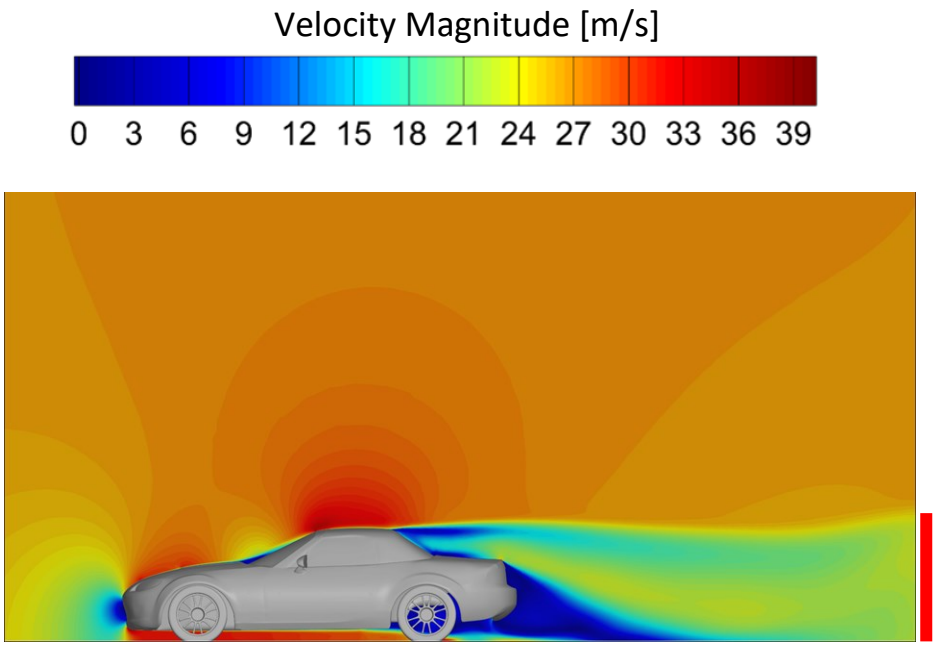

Figure 18. Velocity Contour (*Case I*)

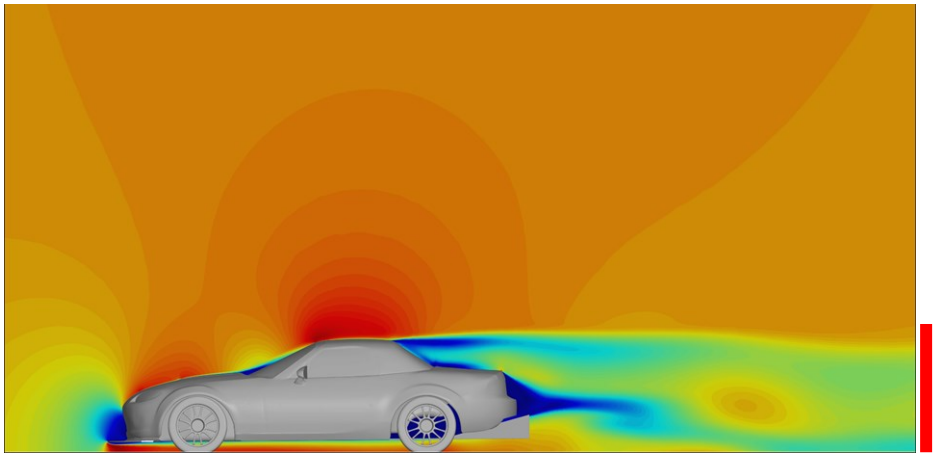
Figure 19. Velocity Contour (*Case II*)

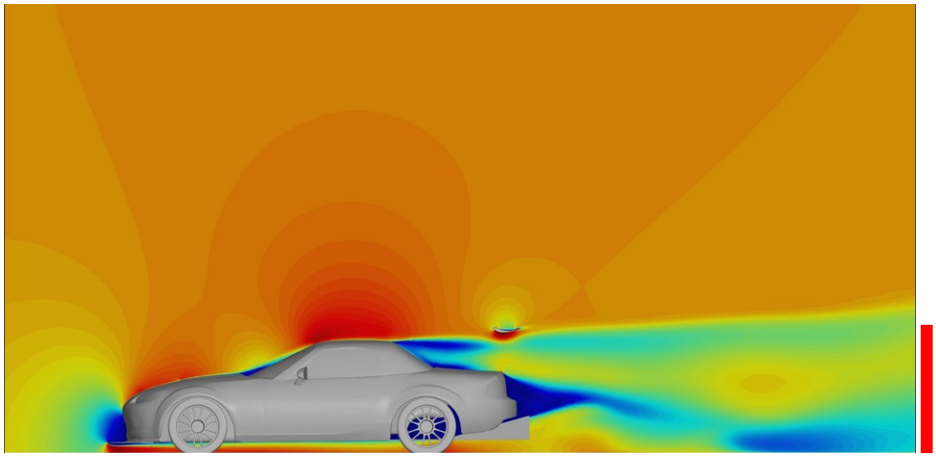
Figure 20. Velocity Contour (*Case III*)

3.2.6 CFD Trends and Pressure Visualization

Pressure coefficient results have been plotted and can be seen in Figure 23 – Figure 24. High-pressure regions are shown in shades of red, and low-pressure regions are shown in shades of blue. Only the unmodified (*Case I*) and modified (*Case III*) are included for the sake of brevity. Pressure gradients remained largely unchanged between *Case II* and *Case III*.

First, a stagnation region can be seen on the leading edge of the front bumper and on the front splitter in *Case III*. It should be noted that flow-through effects of the grille have been neglected on the digital vehicle by smoothing-over the geometry at the air inlet. On the physical car, air is permitted to pass through a honeycomb grill and into the engine bay for cooling and engine aspiration. Flow through effects were neglected in this analysis to reduce complexity and compute time. Some amount of error has been introduced by this assumption, likely in the form of a smaller stagnation region on the physical model. As a result, the physical vehicle is likely to experience less splitter effectiveness than predicted by the digital model.

Second, a flat floor assumption has been applied to the floorboards in all geometry configurations which was also done to reduce model complexity and compute time. As previously noted, a flat floor has been added to *Case II* and *Case III* to span the gap between the passenger floorboards and the diffuser inlet. Care has been taken to avoid suspension and powertrain components, but the exhaust system would need to be reworked to accommodate this design. As a result of these underbody assumptions, the digital model is likely to overpredict downforce when compared to the physical vehicle.

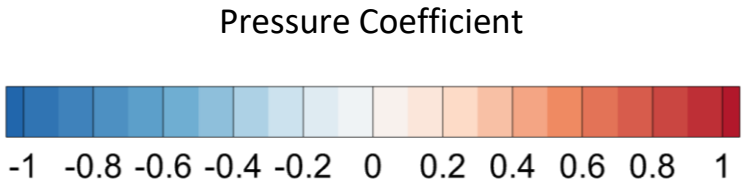

Case I

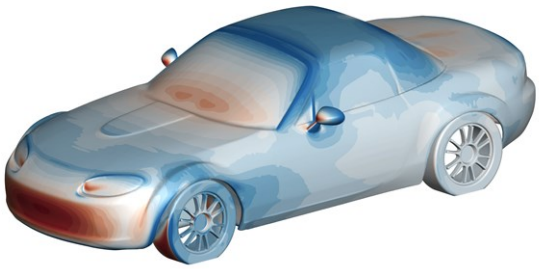

Figure 21. Pressure Coefficient Below

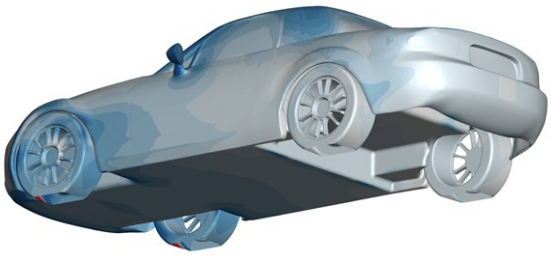

Figure 22. Pressure Coefficient Above

Case III

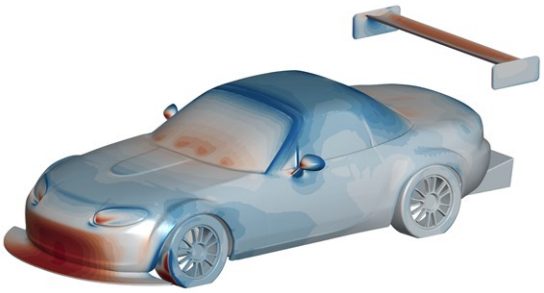

Figure 23. Pressure Coefficient Above

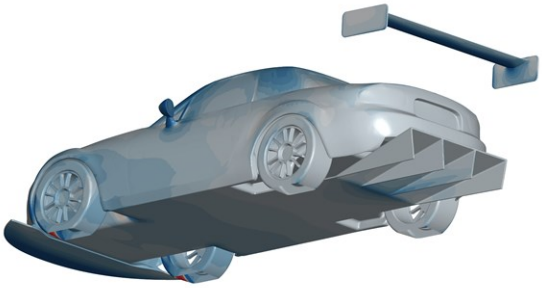

Figure 24. Pressure Coefficient Below

Finally, vorticity iso-surfaces have been plotted with respect to time and flooded with velocity contours. A visualization has been saved for each time-step, and these results have been combined into vorticity animations. The starting and ending frames of each animation can be seen in Figure 25 – Figure 28.

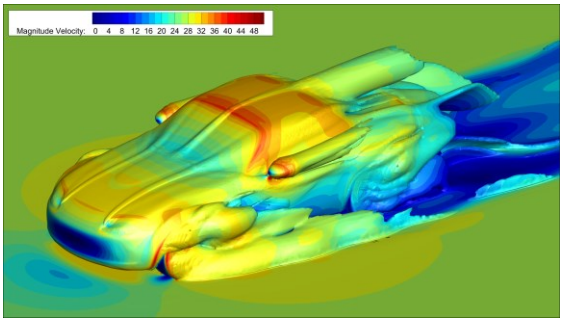

Figure 25. Vorticity Start Frame (*Case I*)

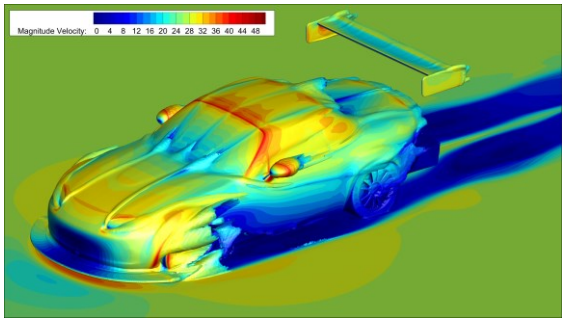

Figure 26. Vorticity Start Frame (*Case III*)

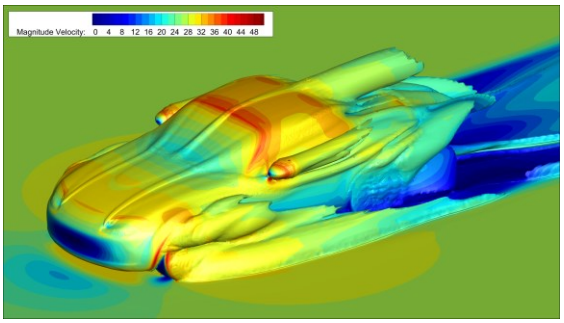

Figure 27. Vorticity End Frame (*Case I*)

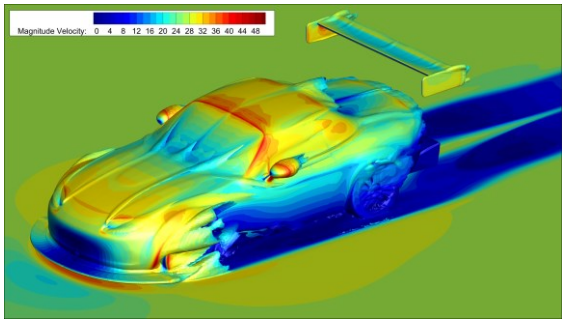

Figure 28. Vorticity End Frame (*Case III*)

4 CONCLUSION

4.1 Contextualizing Results

To place the lift and drag coefficients in a larger context, force coefficients from *Case I* and *Case III* at sixty miles per hour were imported into OptimumLap. This is a free-to-use software program which allows users to import vehicle and racetrack data to predict lap times. In this case, the standard model for the 2006 Mazda Miata, and the circuit model for Roebling Road were imported. Vehicle parameters including redline, gear ratios, final drive ratio, and peak engine torque were verified against the technical specification document published by Mazda [2].

Two cases were initialized on Roebling Road, the first used the lift and drag coefficients from *Case I*, and the second used lift and drag coefficients from *Case III*. The analysis was run, and plots were generated. Aerodynamic downforce can be seen in Figure 29, where a positive downforce (red) indicates a negative lift value and more traction. Conversely, negative downforce values (blue) indicate a lifting force and less traction. The modified vehicle (*Case III*) is shown on the outer loop, and the unmodified (*Case I*) geometry is shown in the inner loop.

Similar to the downforce plot, aerodynamic drag can be seen in Figure 30. Again, *Case III* is shown on the outer loop, and *Case I* is shown on the inner loop. It can be noted that negligible difference exists between the two cases in the drag result. This behavior is expected because of the small 2.8% drag coefficient reduction taken from the tabular results.

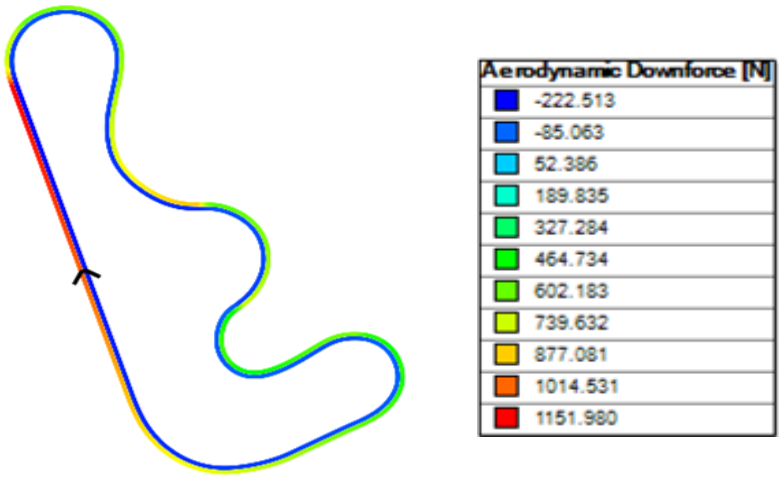

Figure 29. Aerodynamic downforce (*Roebling Road*)

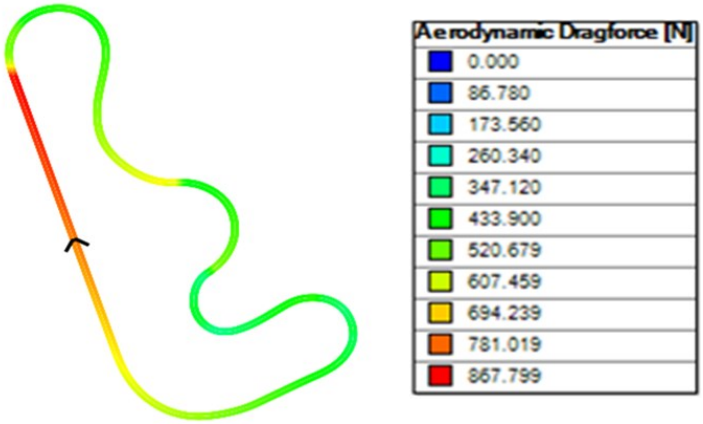

Figure 30. Aerodynamic dragforce (*Roebling Road*)

Finally, lap times were compared across the two configurations. The modified (*Case III*) configuration was predicted to have a lap time 0.65 [s] less than the unmodified (*Case I*) geometry. This marks a significant reduction in a motorsport setting because lap time reduction values accumulate across race duration. For example, in a ten lap race the modified vehicle would finish 6.5 seconds sooner than the unmodified vehicle, all else being equal.

4.2 Closing Remarks

Three conclusions can be drawn from this analysis. First, lap times can be improved by aerodynamic means by as much as 0.65 seconds. This lap time reduction was calculated using OptimumLap based on aerodynamic lift and drag coefficients taken from Table 3. This reduction is significant because changes in lap time accumulate over the course of a motorsports race.

Second, lift and drag can be reduced simultaneously for a 2006 Mazda Miata. Lift coefficient was reduced by a factor of 7 times, and drag coefficient was reduced by 2.8 percent according to the data presented in Table 3. These improvements can be explained by the increase in wake height, and the size reduction of the separation bubble respectively as seen in Figure 18 - Figure 20.

Third, a vehicle's design can be tailored to achieve balance at any speed. A 34% handling improvement was calculated based on the change in moment coefficient from the stock to the modified configuration as presented in Table 3. Furthermore, the stock vehicle was analyzed to become increasingly unstable with respect to velocity. After the addition of aerodynamic modifications, this trend was reversed, and the vehicle was predicted to become increasingly stable at high-speed.

REFERENCES

[1] McBeath, S. (2017). Competition Car Aerodynamics 3rd Edition. Veloce Publishing Ltd.

[2] Mazda Motor Corp. (2005). 2006 Mazda MX-5 Miata Technical Specifications. Mazda USA. https://news.mazdausa.com/download/SPECS-MX5-06.pdf

[3] Emmerling, A. (2008). Autos im Windkanal - AUTO BILD. Autobild.de. https://www.autobild.de/artikel/autos-im-windkanal-666465.html

[4] Forster, K. (2016). 2009 Mazda Miata. cad.onshape.com. https://cad.onshape.com/documents/6a7ca8048ec7d5e46970ea6e/w/d02dd6b947f4456522274647/e/6de9b1f1fbff12cab4248887?renderMode=0&uiState=66272f2ab5ccc77c285bf1fe

[5] Gadola, M., Chindamo, D., Magri, P., & Sandrini, G. (2022). Analyzing Porpoising on High Downforce Race Cars: Causes and Possible Setup Adjustments to Avoid It. Energies, 15(18), 6677. https://doi.org/10.3390/en15186677

[6] Nabutola, K. L., & Boetcher, S. K. S. (2021). Assessment of conventional and air-jet wheel deflectors for drag reduction of the DrivAer model. Advances in Aerodynamics, 3(29). Springer Open. https://doi.org/10.1186/s42774-021-00086-7

[7] Lanfrit, M. (2005, February 9). Best practice guidelines for handling Automotive External Aerodynamics with FLUENT. Southampton University; Fluent Deutschland GmbH. https://southampton.ac.uk/~nwb/lectures/GoodPracticeCFD/Articles/Ext_Aero_Best_Practice_Ver1_2.pdf

[8] SpaceClaim, Corp. (2017). Shrinkwrap. Help.spaceclaim.com. https://help.spaceclaim.com/2017.0.0/en/Content/Shrinkwrap.htm

[9] Ansys, Inc. (2009). *ANSYS FLUENT 12.0 Theory Guide - 1.2 Continuity and Momentum Equations*. Enea.it. https://www.afs.enea.it/project/neptunius/docs/fluent/html/th/node11.htm

[10] Menter, F. (1992). Improved Two-Equation k-omega Turbulence Models for Aerodynamic Flows. In NASA.gov. National Aeronautics and Space Administration. https://ntrs.nasa.gov/api/citations/19930013620/downloads/19930013620.pdf

[11] Pakkam, S. S. (2011). High Downforce Aerodynamics for Motorsports. Repository.lib.ncsu.edu. https://repository.lib.ncsu.edu/items/50c5cde9-889b-44c6-99b9-555e4d25f059

[12] Ansys, Inc. (2009). *Computing Forces, Moments, and the Center of Pressure*. ANSYS Fluent 12.0 Theory Guide; ANSYS. https://www.afs.enea.it/project/neptunius/docs/fluent/html/th/node414.htm